



Developmental Patterning by Mechanical Signals in Arabidopsis

Olivier Hamant, *et al.*
Science **322**, 1650 (2008);
DOI: 10.1126/science.1165594

The following resources related to this article are available online at www.sciencemag.org (this information is current as of May 22, 2009):

Updated information and services, including high-resolution figures, can be found in the online version of this article at:

<http://www.sciencemag.org/cgi/content/full/322/5908/1650>

Supporting Online Material can be found at:

<http://www.sciencemag.org/cgi/content/full/322/5908/1650/DC1>

A list of selected additional articles on the Science Web sites **related to this article** can be found at:

<http://www.sciencemag.org/cgi/content/full/322/5908/1650#related-content>

This article **cites 40 articles**, 13 of which can be accessed for free:

<http://www.sciencemag.org/cgi/content/full/322/5908/1650#otherarticles>

This article has been **cited by** 1 article(s) on the ISI Web of Science.

This article has been **cited by** 1 articles hosted by HighWire Press; see:

<http://www.sciencemag.org/cgi/content/full/322/5908/1650#otherarticles>

This article appears in the following **subject collections**:

Botany

<http://www.sciencemag.org/cgi/collection/botany>

Information about obtaining **reprints** of this article or about obtaining **permission to reproduce this article** in whole or in part can be found at:

<http://www.sciencemag.org/about/permissions.dtl>

Developmental Patterning by Mechanical Signals in *Arabidopsis*

Olivier Hamant,^{1,2*} Marcus G. Heisler,^{3*} Henrik Jönsson,^{4*} Pawel Krupinski,⁴ Magalie Uyttewaal,^{1,2} Plamen Bokov,^{5,6} Francis Corson,⁵ Patrik Sahlin,⁴ Arezki Boudaoud,⁵ Elliot M. Meyerowitz,^{3†} Yves Couder,^{6†} Jan Traas^{1,2†}

A central question in developmental biology is whether and how mechanical forces serve as cues for cellular behavior and thereby regulate morphogenesis. We found that morphogenesis at the *Arabidopsis* shoot apex depends on the microtubule cytoskeleton, which in turn is regulated by mechanical stress. A combination of experiments and modeling shows that a feedback loop encompassing tissue morphology, stress patterns, and microtubule-mediated cellular properties is sufficient to account for the coordinated patterns of microtubule arrays observed in epidermal cells, as well as for patterns of apical morphogenesis.

The surface layers of plant tissues are under considerable tension (1). This results from the fact that individual cells, including those in deeper layers, are tightly bound to each other through their cellulosic walls, on which they exert turgor pressure (2). In addition, plant cell walls resist stress (force per unit area) differentially, depending on the direction of stress (3). This anisotropy is a consequence of the direction in which the rigid cellulose microfibrils are laid down during wall synthesis (4). Because this direction is often parallel to the cortical microtubules of the plant cell, it is thought that the microtubules might serve as tracks along which the cellulose synthase complexes travel (5, 6). Green and others have proposed that cortical microtubule orientations correlate with anisotropic stresses, but the existence of such a causal link with morphogenesis has never been further investigated (7–11). We have chosen to dissect this link in shoot apical meristems, a population of stem cells that continuously generate aerial organs while undergoing complex shape transformations (12, 13) (fig. S1).

Morphogenetic role of the microtubules at the shoot apex. To assess the functional importance of microtubules within the *Arabidopsis* meristem, we depolymerized the microtubules with the use of oryzalin and monitored the resulting cell morphology (14). In the absence of microtubules,

the meristems kept growing but no cytokinesis occurred, and giant polyploid cells formed (Fig. 1A) (14). Despite these changes, differentiation and patterning were not drastically affected. We observed slow-growing cells in the meristem and fast-growing cells in the primordia, and phyllotaxis was not altered 46 hours after complete depolymerization of microtubules (Fig. 1B and fig. S2). Cell identity in the boundary domain between the meristem and new floral primordia did not seem to be altered, as a boundary domain reporter, *pBOUND-GFP*, was induced in this domain several days after the treatment (Fig. 1C and fig. S2).

However, depolymerization of the microtubules resulted in a distinct change in the geometry of the cells. The final structure resembled two-dimensional (2D) foams, which are purely isotropic in nature. Notably, all the walls met at angles of 120° and the curvature of the walls approached that of a soap-bubble network (Fig. 1A) (15, 16). In addition, certain morphogenetic events did not occur. In particular, the crease between the meristem and primordia no longer formed (Fig. 1, B to D, and fig. S2). Hence, although microtubules may not be critical for developmental patterns such as phyllotaxis, they are required for certain morphogenetic events such as tissue folding.

In the presence of oryzalin, organ outgrowth was still observed, which suggests that plant shape is at least partially independent of microtubule-based anisotropy. Because growth patterns are thought to depend largely on the plant hormone auxin (17–21), we next used a double drug treatment where both microtubules and auxin transport were inhibited. This led to the formation of a spherical shoot tip (fig. S3A) (14), as might be expected if microtubule-controlled anisotropy operates in parallel with auxin-driven growth rate patterns.

Cortical microtubule orientations and dynamics are correlated with morphogenesis. To further analyze the role of microtubules in morphogenesis, we investigated microtubule dynamics in the meri-

stem via live imaging of plants expressing green fluorescent protein (GFP) fused to the microtubule-binding domain (MBD) of microtubule-associated protein 4 MAP4 (22, 23). A quantitative analysis of the cortical microtubules at the surface of more than 30 meristems revealed three aspects of microtubular arrays:

1) The microtubules at the meristem summit were highly dynamic, constantly changing their orientation at 1- to 2-hour intervals (Fig. 2, A to C, and movie S1) (24, 25).

2) At the periphery and base of the meristem, orthoradial (circumferential) cortical microtubule arrays were dominant. This orientation was more apparent when organ initiation was inhibited in the presence of the auxin transport inhibitor *N*-1-naphthylphthalamic acid (NPA) and seemed to be the default orientation at the periphery in the absence of floral primordia (fig. S4).

3) As flower primordia started to grow out, a supracellular alignment of microtubules along the boundary between the meristem and the primordium appeared (Fig. 2, A and B, and fig. S4). This configuration was stably maintained over prolonged periods (up to 20 hours). Consistent with these highly ordered and stable interphase arrays, about 90% of the cells ($n = 158$, eight meristems) in this zone displayed preprophase bands and division planes in the same tangential orientation. Microtubules were aligned during the activation of *pFIL::dsRED-N7* (18), a late marker of floral primordium initiation, showing that the alignment accompanies flower outgrowth (Fig. 2D).

Microtubule orientations align along predicted principal stresses. In a multicellular setting, the field of physical forces represents a potential source of information for the cells to know their relative position (7, 26–30). Several studies have supported the proposal that maximal stress directions orient cortical microtubules, most probably via a response to strain in the cell wall (8, 10, 31–33). However, these studies do not address the link with morphogenesis. In addition, it remains difficult to test the plausibility of such a hypothesis in a tissue context. We therefore used a combination of physical and mathematical approaches to address these issues.

To assess whether stresses might orient microtubules, we first calculated the expected pattern of stresses at the shoot apical meristem surface by considering the apex at the tissue scale. Our mechanical model of the meristem as a pressure vessel—a shell inflated by an inner pressure—depends on the following assumptions: (i) The tissue is elastic [(34, 35) and our results], (ii) the outer wall of the epidermal layer supports the turgor pressure and acts as a limiting factor for growth (36, 37), and (iii) the outer wall of the epidermal layer is under a uniform pressure from the inside (34). Using these properties, we calculated the directions of principal stresses in different domains of the shoot apex and found that they are parallel to the observed cortical microtubule orientations (Fig. 3, A and B).

¹INRA, Laboratoire de Reproduction et Développement des Plantes, 46 Allée d'Italie, 69364 Lyon Cedex 07, France.

²Université de Lyon, CNRS, ENS, 46 Allée d'Italie, 69364 Lyon Cedex 07, France. ³Division of Biology, California Institute of Technology, Pasadena, CA 91125, USA. ⁴Computational Biology and Biological Physics Group, Department of Theoretical Physics, Lund University, S-221 00 Lund, Sweden.

⁵Laboratoire de Physique Statistique, Ecole Normale Supérieure, 24 rue Lhomond, 75231 Paris Cedex 05, France. ⁶Matière et Systèmes Complexes, Université Paris-Diderot, 10 rue Alice Domont et Léonie Duquet, 75025 Paris Cedex 13, France.

*These authors contributed equally to this work.

†To whom correspondence should be addressed. E-mail: jan.traas@ens-lyon.fr (J.T.); meyerow@caltech.edu (E.M.M.); couder@lps.ens.fr (Y.C.)

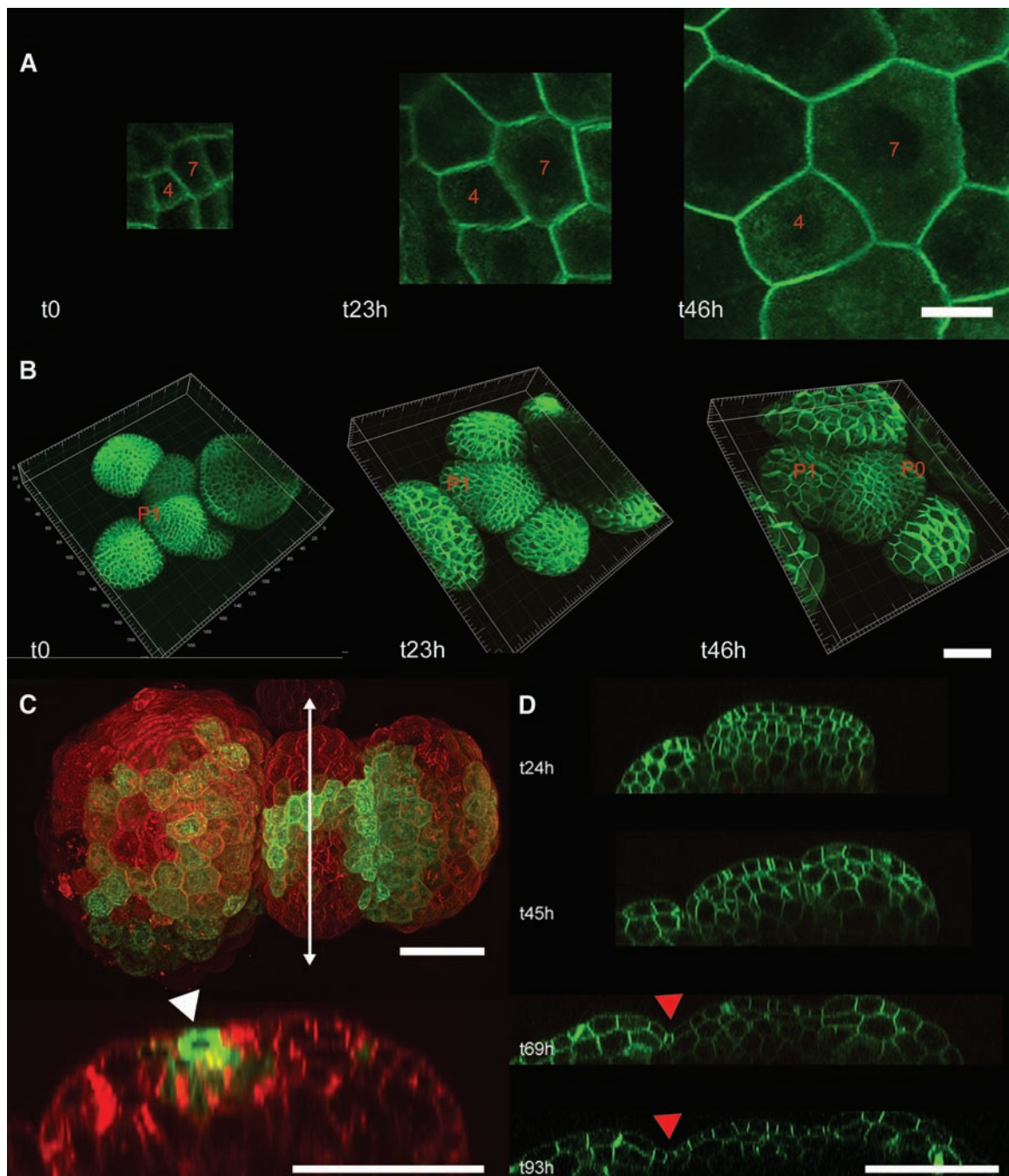
To further investigate the correlation between predicted stresses and microtubule orientations, we designed a 3D cell- and wall-based tissue model representing the surface of the L1 layer of the shoot and incorporating the three assumptions listed above. The model includes mechanisms such as elastic wall mechanics, wall growth, cellular mechanical anisotropy (microfibrils), stress feedback, and growth and proliferation (fig. S5, A and B) (38). Mechanical anisotropy is introduced by defining a microtubule direction within each 2D cell where the stiffness of the wall material increases as the wall becomes more parallel to the direction of the cortical microtubules. Stress feedback is introduced by updating the micro-

tubule directions to align along maximal stress directions, which for one cell is measured by the directional weighted average of its wall stresses. Note that strengthening of the walls (by aligning microfibrils) counteracts the main stress intensity but maintains the main stress direction.

The model faithfully reproduced the orthoradial and random microtubule alignments on synthetic templates of the stem and tip of a dome, respectively, and predicted alignment along the crease for a saddle-shaped template (fig. S6). Simulated microtubule directions in a template extracted from a confocal data set also predicted the experimentally seen boundary alignment zone as well as the more random microtubule orienta-

tions at the apex (Fig. 3C). A growth model was then introduced to examine microtubule orientations during morphogenetic events, including primordium growth and tip growth (38). Primordium growth was initiated by locally decreasing wall stiffness, leading to the outgrowth of a well-defined bump. As the simulated primordium formed, the model also predicted an orthoradial microtubule alignment as observed in the region between the meristem and the primordium (Fig. 3D and movie S2) as well as around the simulated primordium, thus reproducing the alignment zone between the meristem and the primordium. Growth of the meristem and stem was simulated by implementing growth at a rate that was depen-

Fig. 1. Morphogenetic role of the microtubules. **(A)** Effect of oryzalin treatment on cell shape. Walls tend to meet at 120° and become convex or concave in cells with less or more than six walls, respectively, as observed in a 2D foam. Numbers of walls are in red. Scale bar, $10\ \mu\text{m}$. **(B)** Three-dimensional reconstructions of *GFP-LTI6b* meristems treated with oryzalin immediately after the treatment (t0) and 23 and 46 hours later. Note the absence of a crease at P1 and the position of P0 following the expected phyllotactic pattern. Scale bar, $50\ \mu\text{m}$. **(C)** *pBOUND-GFP* (green) expression 3 days after the first oryzalin treatment, in the absence of a crease (arrowhead), in a meristem stained with the fluorescent lipophilic dye FM4-64 (red). Scale bars, $50\ \mu\text{m}$. **(D)** Longitudinal optical sections of an existing crease being flattened over time after oryzalin treatment (red arrowhead). Scale bar, $50\ \mu\text{m}$.



dent on the distance to the apex (Fig. 3E and movie S3) (39). In these simulations, the microtubule orientations were unstable at the apex while the orientations on the stem stabilized in a mainly orthoradial pattern, as was observed. Finally, we tested whether the model could also predict the effects of oryzalin treatment, simulated by removing the anisotropic contribution to wall mechanics. Both a loss of the crease in the experimental template and ballooning of cells in a pin-shaped growth simulation were qualitatively predicted (fig. S3, B and C).

Cell ablation results in characteristic microtubule reorientations. The results so far suggest a scenario where the alignment of microtubules to maximal stress directions modifies the orientation of newly deposited cellulose microfibrils, thereby regulating morphogenesis. We next tested this scenario experimentally.

We began with a laser ablation approach. We reasoned that by killing cells and thereby locally eliminating turgor pressure and weakening cell walls, we could induce characteristic changes in stress and strain patterns. To obtain theoretical predictions for the resultant stress patterns due to laser ablation, we used the finite-element method (FEM) to model the L1 layer of meristem cells (38). The ablation is simulated as a loss of turgor as well as diminution of elastic properties of the walls of the ablated cells (fig. S5C) (38).

The simulation predicts rearrangement of principal stress directions during ablation. Before the removal of the cell, the principal stress patterns depend more on the geometry of each individual cell than on the relationship between cells (Fig. 4A, left). Assuming that the top wall is intact at $t = 0$ hours and gradually weakens afterward, our modeling predicted the maximal stress direction (hence the microtubule orientations) initially to be radial and then to become circumferential with respect to the wound (Fig. 4A).

We used a laser to target cells within the central zone of the meristem, where observed cortical microtubule alignments and growth patterns suggest that cell walls are largely mechanically isotropic. Time-lapse analysis of cells surrounding an ablation site showed a slight initial expansion of surrounding cells into the wound during the first 1.5 hours after laser treatment, consistent with a sudden imbalance in stresses due to loss of turgor in the dead cell or cells (Fig. 4B and movie S4). During this time, no significant microtubule reorientation was detected. However, starting at 1.5 hours and continuing to about 5.5 hours after ablation, we subsequently observed microtubule orientations to align circumferentially (Fig. 4B and movie S4). These results match the predictions of our model and are also consistent with previous reports of circumferential microtubule rearrangements in response to wounding (40, 41). The ab-

sence of an initial radial alignment suggests that the initial stresses associated with radial expansion are too transient to trigger a response.

Although these results support our hypothesis, several alternative hypotheses could not be excluded at this stage. For instance, it is possible that the microtubules may be reorienting perpendicular to the observed initial cell deformations, contrary to our stress alignment proposal. However, because the realignment occurs hours after the initial radial deformation is initiated, this possibility seems less likely. Another hypothesis is that the microtubules may not be responding to mechanical stress but rather to unrelated biochemical wound signals. To test this last scenario, we first proceeded with ablations in the boundary domain. We reasoned that local diffusion of a biochemical signal in this domain and in the central zone should be roughly similar, whereas in the boundary the stress field generated by the ablation should be in competition with the strong tangential stress at the crease (fig. S7, A and B). In contrast to central zone ablations, ablations in boundary regions resulted in a lack of microtubule reorientation in neighboring cells, or a delay of reorientation lasting 7.5 hours or more in some cases. In most cases (five of six experiments), we could find at least one cell with no circumferential microtubule orientation 7.5 hours after ablation, and in two cases, no reorientations

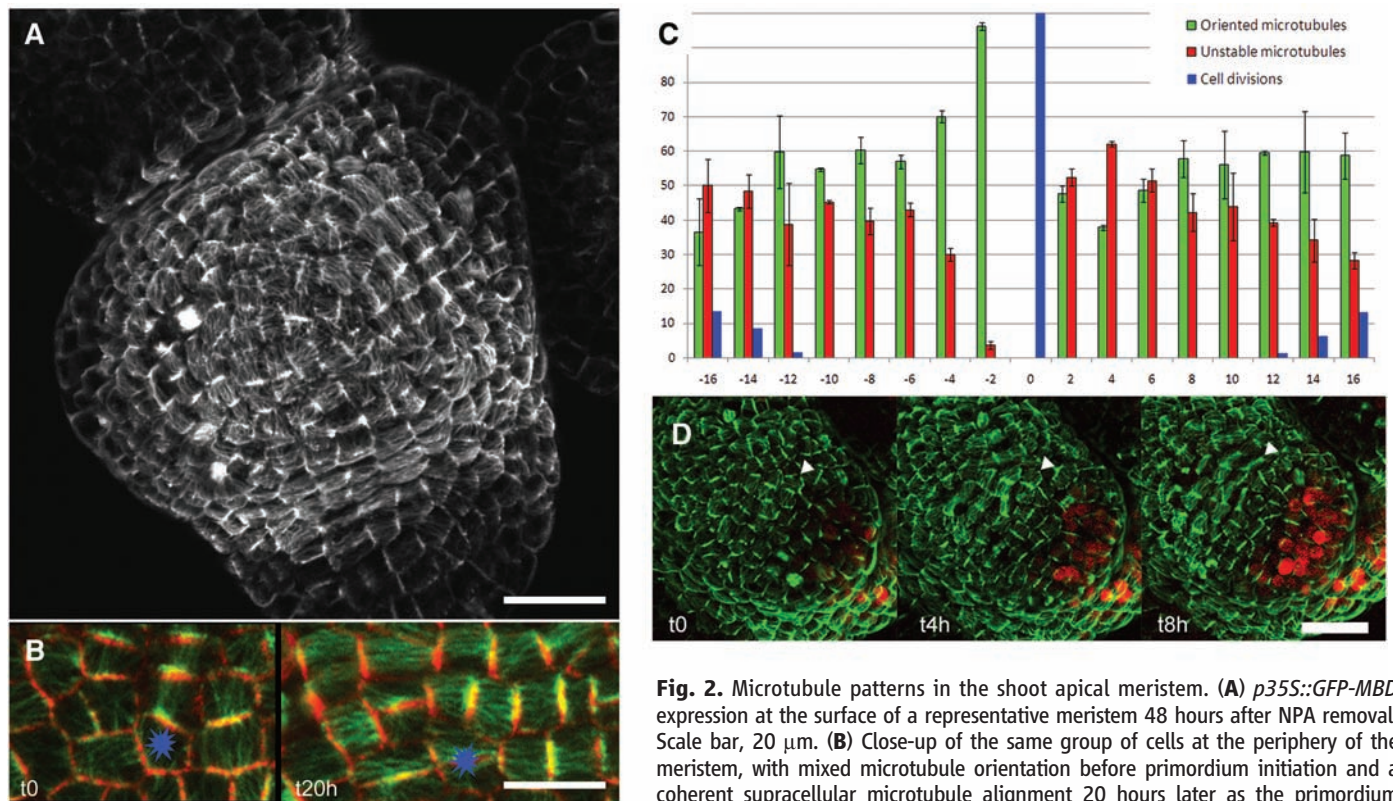


Fig. 2. Microtubule patterns in the shoot apical meristem. **(A)** *p35S::GFP-MBD* expression at the surface of a representative meristem 48 hours after NPA removal. Scale bar, 20 μ m. **(B)** Close-up of the same group of cells at the periphery of the meristem, with mixed microtubule orientation before primordium initiation and a coherent supracellular microtubule alignment 20 hours later as the primordium grows out. The blue star marks the same position in both images. Scale bar, 10 μ m. **(C)** Cortical microtubule behavior in each cell of the meristematic dome every 2 hours for 16 hours before and after cell division ($n = 144$ cells, compiled from five meristems). Blue, percentage of dividing cells at each time point; green, percentage of cells with one major orientation maintained between two time points; red, percentage of cells with a changing microtubule orientation greater than 30° over two time points. **(D)** *p35S::GFP-MBD* (green) and *pFIL::dsRED-N7* (red) expression in the boundary (arrowhead) of a representative meristem at three time points. Scale bar, 20 μ m.

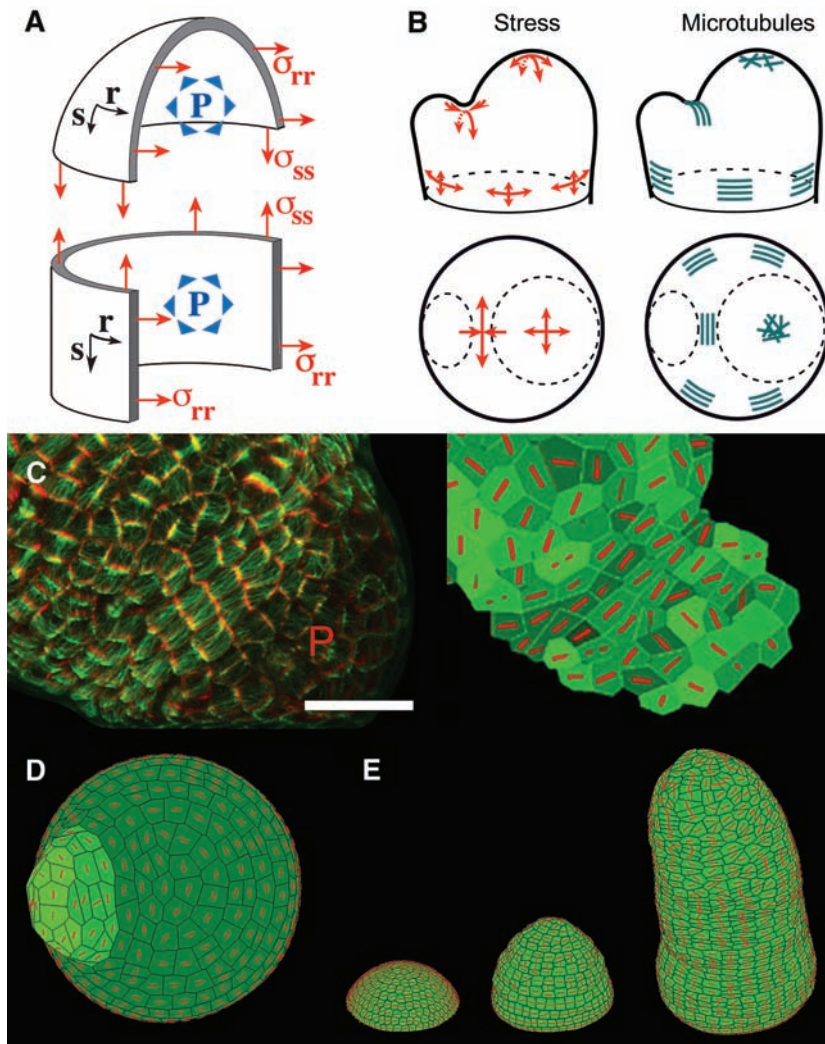


Fig. 3. Physical calculations and modeling of stress patterns in the meristem. **(A)** The meristem modeled as a pressure vessel. Each point has a coordinate in the orthoradial (r) and meridional (s) direction and is characterized by a curvature tensor (C_{ss} , C_{rr} , C_{rs}) and a stress tensor (σ_{ss} , σ_{rr} , σ_{rs}), where R is the radius of the cylindrical stem and of the apical dome, and P is pressure. **(B)** The direction of microtubules is in agreement with the highest-stress orientations. The mechanical equilibrium of the outer layer imposes $\partial_s \sigma_{ss} + \partial_r \sigma_{rs} = 0$, $\partial_s \sigma_{rs} + \partial_r \sigma_{rr} = 0$, and $C_{ss} \sigma_{ss} + C_{rr} \sigma_{rr} + 2C_{rs} \sigma_{rs} = P$, where ∂_s is the partial derivative with respect to s . In the following, we consider only special points (of local symmetry) for which (r, s) are principal directions and $C_{rs} = 0$, $\sigma_{rs} = 0$. If the apical dome is represented as a spherical dome of radius R , we obtain $\sigma_{ss} = \sigma_{rr} = PR/2$, meaning that the stress is isotropic (44). This is correlated with the absence of preferential direction for microtubules in the apical dome. $\sigma_N = PR/2$ serves as a reference for stress and $\delta = |\sigma_{ss} - \sigma_{rr}|/\sigma_N$ as a measure of the anisotropy of stress. We represent the flanks of the meristem as a cylinder of radius R . The stress is greater in the circumferential direction, $\sigma_{rr} = PR$, than along the meridian, $\sigma_{ss} = PR/2$ (44), so that $\delta = 1$, thus leading to a strongly anisotropic stress on the flanks of the meristem. We consider the center of the crease between a primordium and the apex as having radii of curvature R along the axis of the crease, r , and $-\rho$ in the perpendicular direction, s . The minus sign denotes the inverted direction of curvature with respect to the rest of the meristem. The corresponding curvatures are $C_{ss} = -1/\rho$ and $C_{rr} = 1/R$. The equations of equilibrium can be solved in the limit where ρ is small relative to R : $\sigma_{ss} \approx -P\rho/2$ and $\sigma_{rr} \approx PR/2$, so that $\delta \approx 1$, thus leading to a strongly anisotropic stress at the crease between a primordium and the apex. **(C)** Left: $p35S::GFP-MBD$ marking cortical microtubules (green) and cell shape (red) at the surface of a meristem generating a young primordium (P). Scale bar, 20 μm . Right: Microtubule orientation (red bars) in the 2D stress-feedback model on cells extracted from the confocal data, notably reproducing the original microtubule orientations in the boundary. **(D)** Simulation of an auxin-induced primordium. The 2D stress-feedback model results in alignment of microtubules orthoradially around the growing primordium. **(E)** Tip-growing simulation with the stress-feedback model generating a growing stem. Microtubules align mainly orthoradially on the stem, which has a regular shape.

occurred in any of the surrounding cells 7.5 hours after ablation (fig. S7C). The variability of the results could reflect the different stages of boundary development or the exact position of the ablated cells. We also tried a different set of experiments in which two cells or patches of cells, in close proximity but separated, were ablated. We reasoned that diffusion of any type of biochemical signal emanating from the ablated regions would result in a relatively flat diffusion gradient in the regions between them, and therefore that the microtubule arrays in these regions should not be well defined (fig. S8, A and B). In both cases, with ablations separated by multiple cells or single cells, we found that the resulting microtubule orientations for regions between the ablation sites were well defined and clearly circumferential in nature (fig. S8C; four of four experiments). This pattern matches our theoretical predictions for stress patterns surrounding two ablation sites but did not match our prediction for response to a diffusion gradient. Although stress is the simplest explanation, more complex, non-mechanical cell-cell communication models are still possible.

Application of constraints shows a cell-autonomous microtubule response to stress.

To more directly ascertain the relationship between microtubule orientations and mechanical signals, we pursued a second approach involving the direct application of force to the meristem. We designed growth chambers in which meristems could be constrained between one fixed teflon blade and one teflon blade attached to a spring (Fig. 4, C and D). Using this device, we were able to change meristem shape (Fig. 4E and figs. S9A and S10). After the release of the constraint, the meristem reverted to its original shape, showing its elastic properties, and later initiated organs (fig. S9A). We predicted a weakly anisotropic stress larger in the direction parallel to the blades (fig. S10). Consistent with these calculations, only weak anisotropic changes in the shape of individual cells were visible at the meristem summit of the constrained meristems (Fig. 4F and movie S5).

We next analyzed the behavior of the cortical microtubules in each cell before and after the constraint. This revealed that the number of cells with unstable microtubules decreased relative to observations of nonconstrained meristems (Fig. 4G, green histograms, and figs. S9B and S10). Second, an analysis of microtubule orientation in 489 individual cells from 13 compressed meristems showed that most cells reoriented their microtubules toward the axis parallel to the blades, either by stabilizing an orientation parallel to the blades after compression or by rotating their microtubules parallel to the blades (Fig. 4F, figs. S10 and S11, and movies S5 and S6). These data are consistent with our proposal that microtubules align parallel to maximal stress directions. Although the response was statistically significant under the conditions tested here, it was also a noisy response because even neighboring cells can have micro-

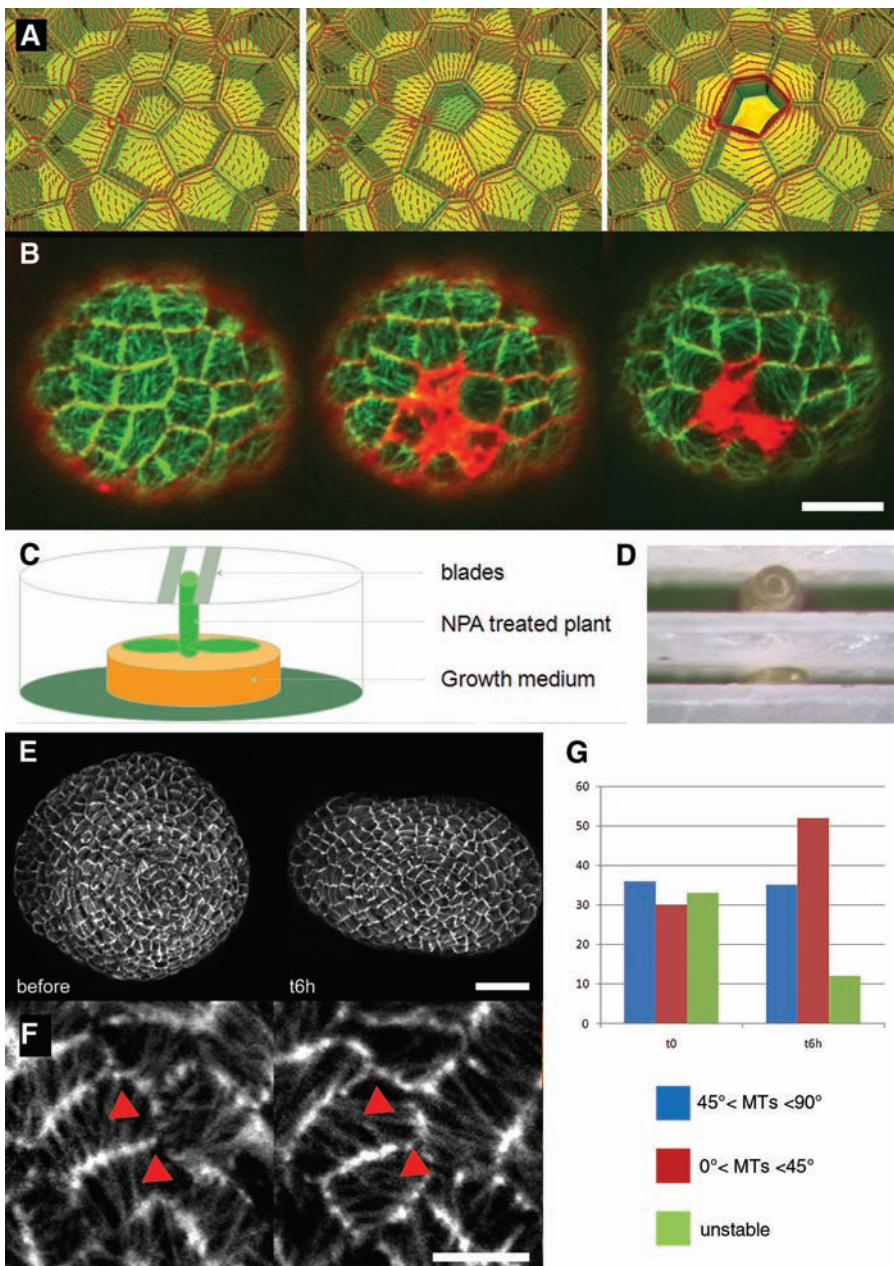


Fig. 4. Reorientation of the cortical microtubules in the presence of a mechanical stress. **(A)** Theoretical principal stress direction pattern (red lines) in outer surface of meristem tissue obtained from FEM simulation of L1 layer under uniform tension and turgor pressure, before and after ablation. Color gives relative values of maximal stress (green, low; red, high). Left: A stress pattern in a group of reference cells. Middle: Radial stresses after the drop of turgor in an ablated cell at the center. Right: Circumferential stresses after the weakening of the top wall. **(B)** GFP-MBD expression (green) in the L1 layer of the central zone of a meristem just before, just after, and 6 hours 30 min after ablation (FM4-64 staining in red). Scale bar, 10 μ m. **(C)** Schematic drawing of the setup used to apply lateral constraints onto the meristem. **(D)** An NPA-treated plant with a naked meristem is put between two blades, and the blades are then adjusted to compress the apex. **(E)** GFP-MBD expression in the L1 layer of a meristem before the application of the constraint (left) and 6 hours (right) after the application of the constraint. Scale bar, 20 μ m. **(F)** Close-up showing the microtubule reorientations before and after the application of the constraint. Arrowheads mark cells where microtubules have reoriented parallel to the blades. Scale bar, 5 μ m. **(G)** Six hours after the application of the constraint, the number of cells with unclear microtubule orientation (green) is decreasing while the number of cells with microtubules having an angle greater than 45° (blue) remains relatively stable and the number of cells with microtubules having an angle less than 45° with the blades (red) is increasing; t0 corresponds to 0 hours after compression. This tendency to alignment matches the predicted weak anisotropy of stress (see fig. S10).

tubules with radically different orientations (Fig. 4F and movie S5). We propose that this variability reflects the cell-autonomous nature of the response and that this follows from the likely different mechanical configurations of different plant cells.

Concluding remarks. We have described a link between mechanical forces and development in plants. Recent work has also revealed such a relation in animals. In particular, the phenomenon of wound-induced actin alignment in epithelial sheets closely parallels the alignment of plant microtubules around a wound, with both responses presumably functioning to reduce or heal tissue damage (42). Unlike animals, however, plant tissues seem to react to oriented forces by conferring anisotropic properties to their extracellular matrix. As a result, plant tissues seem to react to mechanical forces as solids, whereas animal tissues react as fluids. From a physical perspective, this points to a basic difference between the two kingdoms.

On the basis of our results, we propose that two fundamental regulatory circuits control plant morphogenesis at the shoot apex. First, a microtubule-dependent, cell-autonomous mechanism mechanically reinforces cells against maximal tension directions along the meristem surface, most likely via the regulation of load-bearing cellulose fiber deposition and by the addition of new walls generated by oriented mitosis in these directions. This mechanism is required for specific morphogenetic events such as tissue folding and the maintenance of a cylindrical stem. However, in contrast to previous proposals (36, 43), this stress-dependent control of morphogenesis at the meristem can be uncoupled from the control of differential expansion rates, because the rapid outgrowth of organs at particular locations continues despite microtubule depolymerization. This second process involves the creation of differential auxin concentrations through polar transport and possibly synthesis (17–21). We therefore propose that auxin-dependent patterning operates at least partially independently of, and in parallel to, the microtubule-controlled anisotropy. Our experimental results and models show that these two mechanisms are sufficient to explain all observed complex shape changes at the meristem.

References and Notes

1. W. S. Peters, A. D. Tomos, *Ann. Bot.* **77**, 657 (1996).
2. P. Schopfer, *Am. J. Bot.* **93**, 1415 (2006).
3. E. S. Castle, *J. Cell. Comp. Physiol.* **10**, 113 (1937).
4. D. J. Cosgrove, *Plant Physiol. Biochem.* **38**, 109 (2000).
5. G. O. Wasteneys, M. E. Galway, *Annu. Rev. Plant Biol.* **54**, 691 (2003).
6. A. R. Paredez, C. R. Somerville, D. W. Ehrhardt, *Science* **312**, 1491 (2006); published online 20 April 2006 (10.1126/science.1126551).
7. P. B. Green, A. King, *Aust. J. Biol. Sci.* **19**, 421 (1966).
8. R. E. Williamson, *Aust. J. Plant Physiol.* **17**, 601 (1990).
9. A. L. Cleary, A. R. Hardham, *Plant Cell Physiol.* **34**, 1003 (1993).
10. C. L. Wymer, S. A. Wymer, D. J. Cosgrove, R. J. Cyr, *Plant Physiol.* **110**, 425 (1996).
11. K. Fischer, P. Schopfer, *Plant J.* **15**, 119 (1998).
12. J. Traas, J. H. Doonan, *Int. Rev. Cytol.* **208**, 161 (2001).
13. D. Kwiatkowska, J. Dumais, *J. Exp. Bot.* **54**, 1585 (2003).
14. O. Grandjean *et al.*, *Plant Cell* **16**, 74 (2004).

15. C. W. J. Beenakker, *Phys. Rev. Lett.* **57**, 2454 (1986).
16. J. A. Glazier, S. P. Gross, J. Stavans, *Phys. Rev. A* **36**, 306 (1987).
17. D. Reinhardt *et al.*, *Nature* **426**, 255 (2003).
18. M. G. Heisler *et al.*, *Curr. Biol.* **15**, 1899 (2005).
19. P. B. de Reuille *et al.*, *Proc. Natl. Acad. Sci. U.S.A.* **103**, 1627 (2006).
20. H. Jönsson, M. G. Heisler, B. E. Shapiro, E. M. Meyerowitz, E. Mjølness, *Proc. Natl. Acad. Sci. U.S.A.* **103**, 1633 (2006).
21. R. S. Smith *et al.*, *Proc. Natl. Acad. Sci. U.S.A.* **103**, 1301 (2006).
22. S. Sakaguchi, T. Hogetsu, N. Hara, *Bot. Mag. (Tokyo)* **101**, 497 (1988).
23. J. M. Selker, *Protoplasma* **158**, 95 (1990).
24. Z. Hejnowicz, *Protoplasma* **225**, 243 (2005).
25. J. Chan, G. Calder, S. Fox, C. Lloyd, *Nat. Cell Biol.* **9**, 171 (2007).
26. P. M. Lintilhac, in *Positional Controls in Plant Development*, P. W. Barlow, D. J. Carr, Eds. (Cambridge Univ. Press, Cambridge, 1984), pp. 83–105.
27. J. Dumais, C. R. Steele, *J. Plant Growth Regul.* **19**, 7 (2000).
28. E. Farge, *Curr. Biol.* **13**, 1365 (2003).
29. L. Hufnagel, A. A. Teleman, H. Rouault, S. M. Cohen, B. I. Shraiman, *Proc. Natl. Acad. Sci. U.S.A.* **104**, 3835 (2007).
30. T. Lecuit, P. F. Lenne, *Nat. Rev. Mol. Cell Biol.* **8**, 633 (2007).
31. J. M. Hush, R. L. Overall, *Cell Biol. Int. Rep.* **15**, 551 (1991).
32. R. E. Williamson, *Int. Rev. Cytol.* **129**, 135 (1991).
33. R. J. Cyr, *Annu. Rev. Cell Biol.* **10**, 153 (1994).
34. Z. Hejnowicz, in *Pattern Formation in Biology, Vision and Dynamics*, A. Carbone, M. Gromov, P. Prusinkiewicz, Eds. (World Scientific, Singapore, 2000), pp. 240–251.
35. C. Wei, P. M. Lintilhac, J. J. Tanguay, *Plant Physiol.* **126**, 1129 (2001).
36. J. M. Selker, G. L. Steucek, P. B. Green, *Dev. Biol.* **153**, 29 (1992).
37. S. Savaldi-Goldstein, J. Chory, *Curr. Opin. Plant Biol.* **11**, 42 (2008).
38. See supporting material on Science Online.
39. J. Dumais, S. L. Shaw, C. R. Steele, S. R. Long, P. M. Ray, *Int. J. Dev. Biol.* **50**, 209 (2006).
40. J. M. Hush, C. R. Hawes, R. L. Overall, *J. Cell Sci.* **96**, 47 (1990).
41. K. C. Goodbody, C. Lloyd, *Protoplasma* **157**, 92 (1990).
42. P. Martin, J. Lewis, *Nature* **360**, 179 (1992).
43. L. F. Hernandez, P. B. Green, *Plant Cell* **5**, 1725 (1993).
44. W. Flugge, *Stresses in Shells* (Springer-Verlag, New York, ed. 2, 1973).
45. We thank A. Roeder for critical reading of the manuscript, and P. Barbier de Reuille and IFR128 Platim for help with imaging. Supported by the International Human Frontier Science Program Organization, by U.S. Department of Energy grant FG02-88ER13873 (E.M.M.), by the Balzan Foundation (E.M.M.), and by the Swedish Research Council (H.J.).

Supporting Online Material

www.sciencemag.org/cgi/content/full/322/5908/1650/DC1

Materials and Methods

SOM Text

Figs. S1 to S11

Movies S1 to S6

References

8 September 2008; accepted 14 November 2008

10.1126/science.1165594

A Competitive Inhibitor Traps LeuT in an Open-to-Out Conformation

Satinder K. Singh,¹ Chayne L. Piscitelli,^{1,3} Atsuko Yamashita,^{4*} Eric Gouaux^{1,2}

Secondary transporters are workhorses of cellular membranes, catalyzing the movement of small molecules and ions across the bilayer and coupling substrate passage to ion gradients. However, the conformational changes that accompany substrate transport, the mechanism by which a substrate moves through the transporter, and principles of competitive inhibition remain unclear. We used crystallographic and functional studies on the leucine transporter (LeuT), a model for neurotransmitter sodium symporters, to show that various amino acid substrates induce the same occluded conformational state and that a competitive inhibitor, tryptophan (Trp), traps LeuT in an open-to-out conformation. In the Trp complex, the extracellular gate residues arginine 30 and aspartic acid 404 define a second weak binding site for substrates or inhibitors as they permeate from the extracellular solution to the primary substrate site, which demonstrates how residues that participate in gating also mediate permeation.

Secondary active transporters are ubiquitous integral membrane proteins that couple the potential energy stored in preexisting ion gradients to the concentrative uptake of polar and charged molecules across the lipid bilayer of the cell (1–3). Members of the solute carrier 6 (SLC6) family of sodium-coupled transporters, also known as neurotransmitter sodium symporters, make up one of the most widely investigated and pharmacologically important classes (4, 5). SLC6 proteins play a central role in diverse physiological processes, ranging from the maintenance of cellular osmotic pressure (6) to the reuptake of small-molecule neurotransmit-

ters in the brain (7). SLC6 dysfunction is implicated in numerous debilitating illnesses, such as depression (8), obsessive-compulsive disorder (9), epilepsy (10), autism (11), orthostatic intolerance (12), X-linked creatine-deficiency syndrome (13), and retinal degeneration (14). The transport activity of these molecular machines can be inhibited by many different compounds, including tricyclic antidepressants (TCAs) (15), selective serotonergic reuptake inhibitors (15), anti-convulsants (16), and cocaine (17).

Unraveling the molecular principles that define a substrate (a molecule that can be transported) versus a competitive inhibitor (a molecule that can displace the substrate but is not itself transported) is intimately linked to the larger goal of elucidating transport mechanism and ultimately to the development of new therapeutic agents. The leucine transporter (LeuT), a prokaryotic SLC6 member (18), provides an opportunity to couple functional and structural data to uncover the molecular mechanisms of transport and inhibition. Recently, a model for noncompetitive inhibition was derived from a combination of steady-state kinetics (19), binding,

and crystallographic studies with LeuT and three TCAs (19, 20). The structures of LeuT bound to the TCAs clomipramine (19), imipramine (19), or desipramine (19, 20) revealed that each of these drugs binds to LeuT in the extracellular vestibule, about 11 Å above the substrate and directly above the extracellular gating residues R30 and D404 (19–21), stabilizing the occluded state in a closed conformation. Zhou *et al.* have proposed that the TCA-binding site observed in LeuT is equivalent to the primary TCA site in the serotonin transporter (SERT) and the norepinephrine transporter (NET), the therapeutic targets in humans. However, in SERT and NET, TCAs are competitive inhibitors (22–24), and their binding site probably overlaps with the substrate-binding site (25). Therefore, we suggest that the LeuT-TCA complexes do not provide a model for competitive inhibition of eukaryotic SLC6 transporters.

Here we show that LeuT is capable of transporting many hydrophobic amino acids and that a fundamental requirement for a molecule to be a substrate is that it must fit within the occluded substrate-binding cavity. Molecules such as tryptophan (Trp) that can bind but are too large to be accommodated within the occluded-state cavity are not substrates but instead are competitive nontransportable inhibitors. Structural analysis of the LeuT-Trp complex reveals that Trp traps LeuT in an open-to-out conformation and unveils the movements that accompany transition from the occluded to an open-to-out state. Molecular insights gleaned from our studies are especially relevant to the transporter mechanism because many other transporter families, including SLC5 (26), have the same fold as LeuT and probably share mechanistic principles.

Substrate screen of LeuT. To identify a competitive inhibitor of LeuT, we examined the ability of a spectrum of amino acids to displace [³H]Leu binding from purified detergent-solubilized LeuT and inhibit [³H]Leu transport by LeuT reconstituted into lipid vesicles (Fig.

¹Vollum Institute, Oregon Health and Science University, 3181 Southwest Sam Jackson Park Road, Portland, OR 97239, USA.

²Howard Hughes Medical Institute, Oregon Health and Science University, 3181 Southwest Sam Jackson Park Road, Portland, OR 97239, USA. ³Department of Biochemistry and Molecular Biology, Oregon Health and Science University, 3181 Southwest Sam Jackson Park Road, Portland, OR 97239, USA. ⁴Department of Biochemistry and Molecular Biophysics, Columbia University, New York, NY 10032, USA.

*Present address: RIKEN SPring-8 Center, 1-1-1, Kouto, Sayo, Hyogo 679-5148, Japan.